J Therm Spray Tech (2025) 34:1489–1506
https://doi.org/10.1007/s11666-025-01944-2

ORIGINAL RESEARCH ARTICLE

Repair of Single-Crystal CMSX-4 Using the High Velocity Air Fuel Process

M. Létang[1] · S. Björklund[2] · S. Joshi[2] · D. Sebold[1] · O. Guillon[1,3] · R. Vaßen[1,4]

Submitted: 22 July 2024 / in revised form: 3 January 2025 / Accepted: 13 January 2025 / Published online: 24 February 2025

Abstract Turbine blades in aircraft engines and land-based gas turbines are exposed to harsh environmental conditions that make them susceptible to degradation mechanisms, such as creep, oxidation, and fatigue damage. Therefore, research into effective repair methods is of high importance, especially for single crystal components, as they are cost-intensive to produce. The HVAF process is suitable for repair applications as it can produce dense layers with low oxygen content, which are essential for the repaired area. Additionally, the fine grain structure is advantageous for the subsequent directional recrystallization planned in future studies, aiming to transform the repair layer into a columnar or even single-crystal structure. This study focuses on applying CMSX-4 powder to single crystal substrates of similar composition using High Velocity Air Fuel Spraying (HVAF). Specifically, the effects of powder particle size, nozzle configuration, and various other process parameters, such as spray distance and carrier gas flow, on the characteristics of HVAF-deposited CMSX-4 were investigated. The microstructure was examined by scanning electron microscopy. Particle velocity and temperature measurements were performed to enhance comprehension of the process.

✉ M. Létang
m.letang@extern.fz-juelich.de

[1] Institute of Energy Materials and Devices (IMD-2), Forschungszentrum Jülich GmbH, 52425 Jülich, Germany

[2] University West, 46186 Trollhättan, Sweden

[3] Jülich Aachen Research Alliance: JARA Energy, 52425 Jülich, Germany

[4] Institut für Werkstoffe, Ruhr-Universität Bochum, Bochum, Germany

Keywords accura spray · high velocity air fuel spraying · parameter influence · particle temperature and velocity measurements · repair process · single crystal CMSX-4 · single splat

Introduction

Gas turbines are essential in various industrial applications such as power generation and aviation, operating in environments characterized by extreme temperatures, pressures, and contaminants. Turbine blades, positioned directly after the combustion chamber, endure high thermal and mechanical stresses. They are typically manufactured from nickel-based alloys, such as CMSX-4, to withstand these extreme conditions. The beneficial properties of these alloys can be attributed to the specific γ/γ' microstructure. Moreover, because these blades are single crystal, the absence of grain boundaries significantly improves the properties of these materials. Despite their resilience, these blades are susceptible to various forms of damage, including erosion, oxidation, and corrosion at the blade edges due to reactions with combustion gases (Ref 1, 2).

Turbine blades can cost up to $ 8000 per piece, and the value of a full set of high pressure turbine blades, comprising between 60 to 80 blades, ranges from $ 400,000 to $ 700,000 (Ref 3). Single crystal turbine blades in the first stage of the high-pressure turbine are rejected during engine inspection whenever cracks, dimensional discrepancies, hot corrosion attack, or creep are detected (Ref 4). Given the expense and time required to produce single-crystal turbine blades, the development of repair options is economically desirable. Repairing damaged blades can extend their operational life and reduce overall replacement costs. However, the challenge in repairing single-crystal

components lies in preserving the single- crystal microstructure in the substrate and developing a single-crystal microstructure in the deposited material during the repair process. For example, blade tip repairs are currently carried out using welding processes in combination with other materials, resulting in polycrystalline repair areas with poorer mechanical properties (Ref 5). At the moment, there is no adequate repair method available for single-crystal components (Ref 6).

Gäumann et al. (Ref 7, 8) were the pioneers in Epitaxial Laser Metal Forming (E-LMF), marking the successful development of single-crystal repair coatings on a single-crystal substrate. Other studies, such as those by Vilar (Ref 9, 10), demonstrate that precise control in various laser cladding processes facilitates the repair of single-crystal materials. These methods introduce localized heat, enabling a high temperature gradient and rapid solidification, thus enabling epitaxial growth. Various other studies show that laser-assisted processes are interesting for the repair of single-crystal components. Nevertheless, problems such as cracking and stray grain formation still occur. (Ref 11–15)

In general, thermal spray is a promising approach for the repair of gas turbine components (Ref 16–19). Kalfhaus et al. (Ref 20, 21) have demonstrated that the vacuum plasma spraying (VPS) process can be used to deposit thick polycrystalline CMSX-4 repair coatings on a single crystal Nickel-based superalloy. Through subsequent hot isostatic pressing (HIP), porosity was reduced, and grains exhibited growth. Directional temperature gradients resulted in columnar grains. Abnormal grain growth was observed at temperatures slightly above the γ'-solvus temperature.

The high velocity air fuel spraying (HVAF) process is becoming increasingly attractive for the thermal spray industry and is attracting more and more attention in research. This is mainly due to the following reasons: (1) The HVAF process produces high particle velocities at moderate particle temperatures, avoiding negative aspects of any kind of thermally driven degradation of feedstock, such as decarburization. (2) Due to the high kinetic energy, dense coatings can be produced. (3) By using air instead of oxygen as in the high velocity oxygen fuel (HVOF) process, costs can be reduced, and high oxidation of the feedstock can be avoided, enabling the use of finer powders. These advantages make this process an attractive repair method (Ref 22–24).

In this process, a combustion-driven gas stream accelerates powder particles to high velocities. Depending upon the powder material, these particles impact the substrate surface in molten/semi-molten state, forming a dense and well-bonded coating. As a crucial component of an HVAF thermal spray gun, the de Laval nozzle significantly influences the coating's quality by regulating particle behavior during the spraying process. Efficient control over particle heating and acceleration is achieved through different de Laval nozzle geometries. The particle size/mass also has an influence on the particle velocity and, thus, also on the particle temperature at impact (Ref 22, 25, 26).

Owoseni et al. (Ref 27) employed the HVAF process for the repair of Ti-6Al-4V using powder of the same composition. The results indicated that the density of the coatings was high, with the densest coatings exhibiting less than 0.5% porosity. Moreover, these coatings performed well under both sliding and erosion wear conditions, comparable to Ti-6Al-4V bulk material. Another study (Ref 28) explored the suitability of the Inner Diameter-High Velocity Air Fuel (ID-HVAF) process as a repair method for Ti-6Al-4V. However, in this case the phases were not retained, and the produced samples were not as dense as those manufactured with cold spray. Baiamonte et al. (Ref 29) investigated the hand- held HVAF process to support on-site repairs for carbide rich coatings in plants using pure biomass. The results achieved are comparable with the current state of the art and demonstrate the high potential of the HVAF process for repair. However, there are comparatively few studies in the literature that analyze the suitability of HVAF as a repair process.

This study aims to investigate the suitability of the HVAF process as repair process for single crystal components. The process may be particularly suitable as it can produce dense layers with low oxygen content, which is crucial for repair applications. Moreover, the grain size of the coatings is small, which is beneficial because a fine microstructure serves as the driving force for directed recrystallization. Repaired areas should exhibit minimal defects to enable effective directional recrystallization and to ensure favorable mechanical properties. Therefore, this study initially focuses on a parameter study to optimize the coating microstructure. For this purpose, CMSX-4 alloys are selected as substrate and coating materials. Two powder fractions of different particle sizes are investigated using different nozzle configurations. For a better understanding of the process, particle velocities and temperatures were measured, and single splat experiments were carried out. The investigation focused on examining the resulting microstructures by analyzing processing parameters, such as spray distance, powder feed rate, carrier gas flow, and surface speed. As the repair coating is polycrystalline in the as-sprayed condition, it should be converted into a single crystal by means of directional recrystallisation treatment following these investigations. There are already several studies (Ref 30–32) in the literature that have successfully applied this method to produce columnar or single-crystal grain structures. For this purpose, the goal is to produce a dense coating with a low oxide content.

Experimental Methods

Sample Preparation

Both the single-crystal substrate and the feedstock powder material used in this study are CMSX-4 alloys, which are used as turbine blade materials in gas turbines. The composition of the substrate material and the two different powders, as determined by inductively coupled plasma mass spectrometry (ICP-MS) (iCAP 7600 Thermo Fisher Scientific, USA), are given in Table 1. The substrates were machined to a size of 25 × 25 × 3 mm by wire electrical discharge machining and were hot grit blasted before coating, resulting in a Ra of 5.3 µm ± 0.2 µm. For grit blasting, the HVAF gun was operated using a 4L4 nozzle, with the air pressure set to 0.7594 MPa, Fuel 1 pressure set to 0.6895 MPa, and Fuel 2 pressure set to 0.5516 MPa. Al_2O_3 particles with an F36 grain size of 425-600 µm were used. The spray distance was 300 mm, the surface velocity was 100 m/min, and the grit feed rate was 100 g/min. The carrier gas flow rate was 60 L/min. An optical profilometer (CT350T, cyberTECHNOLOGIES GmbH, Germany) was used to measure the roughness of the substrates.

TLS Technik GmbH & CO Spezialpulver KG produced the two powders by gas atomization and then vibration-sieved them to obtain the two different particle size distributions. SEM images of the two powders are shown in Fig. 1. A magnified powder cross-section of the coarse powder is shown in Fig. 1(c). It can be observed that the powder is dense and exhibits a dendritic structure. In the interdendritic regions, bright white precipitates are visible in the SEM, which may correspond to the topologically close packed (TCP) phases present in the material. These phases are further investigated in a separate study. The particle size distribution, measured by laser diffractometry on the LB550 device (Horiba, Japan), and the oxygen content, measured with the LECO ON836 (LECO Corporation, USA) of the powders are given in Table 2.

The coated specimens were manufactured at University West (Trollhättan, Sweden) using a HVAF system with a M3 torch from Uniquecoat Technologies (Oilville, VA, USA). To reach maximum temperatures, a double nozzle system was employed Fig. 2(a). Propane served as the process gas. A rotating carousel was used to mount multiple samples for coating, and continuous cooling of the samples was provided.

In a first step, the influence of different secondary ceramic nozzle configurations at two different pressure settings were investigated. First, the use of lower pressure on air, fuel 1, and fuel 2 was investigated (Table 3 HVAF P1-P4 and P9-P12). Afterward, higher pressures for all 3 gases were utilized to examine the contrast (Table 3 HVAF P5-P8 and P13-P16). The nozzles have been tested with both fine and coarse powder. A sketch of the different convergent-divergent nozzle geometries is given in Fig. 2(b). The nozzles 4L4 and 5L4 have a larger outlet diameter compared to the nozzles 4L2 and 5L2 and thus, a larger expansion ratio. The expansion ratio, defined as the ratio between the nozzle exit diameter and throat diameter (19 mm), is 1.18 for the 4L2 and 5L2 nozzles, while it is 1.36 for the 4L4 and 5L4 nozzles. The 5L2 and 5L4 nozzles are 50 mm longer in the divergent section than the 4L2 and 4L4 nozzles. This allows different particle temperatures and velocities to be realized.

An overview of these trials is given in Table 3. A spray distance of 300 mm and a powder carrier gas flow of 45 L/min were used for these tests. The surface speed for the coating production was 100 m/min and the CMSX-4 powder was fed at 100 g/min. The coatings were carried out in 15 coating passes with a step size of 5 mm. Single splat samples were also prepared in order to gain a better understanding of the particle states at the moment of impact (molten, semi-molten, softened) when using the different nozzles. For splat collection, the single crystal substrates were ground with a SiC paper (grit size P2500) before coating. Moreover, the feed rate was reduced to 20 g/min, the surface speed was increased to 150 m/min, to ensure that isolated splats could be collected during a single pass for careful examination.

Based on all the previous experiments, the 5L4 nozzle in combination with the high pressure settings (air pressure 0.78 MPa, fuel 1 pressure 0.72 MPa and fuel 2 pressure 0.79 MPa) and the fine powder (HVAF P8) were selected for further tests (Table 4). The influence of spray distance, surface speed, carrier gas flow and powder feed rate on the porosity, the oxygen content and the coating thickness were investigated. If necessary, the number of passes was adjusted to obtain a comparable coating thickness. In certain experiments, particle temperatures and velocities were measured using the Accuraspray system. A measurement at different surface speeds would not make sense, as this has no effect on the particle state.

Table 1 Chemical composition in wt.% of the materials used

Name/Element	Ni	Co	Cr	Al	W	Re	Ta	Ti	Mo	Hf
CMSX-4 (substrate)	Bas.	9.6	6.4	5.6	6.4	2.9	6.5	1	0.6	0.1
CMSX-4 powder (25-45 µm)	Bas.	9.3	6.4	5.4	6.3	2.8	6.1	1	0.6	0.1
CMSX-4 powder (< 25 µm)	Bas.	9.1	5.9	5.6	5.7	2.7	5.7	1	0.6	0.1

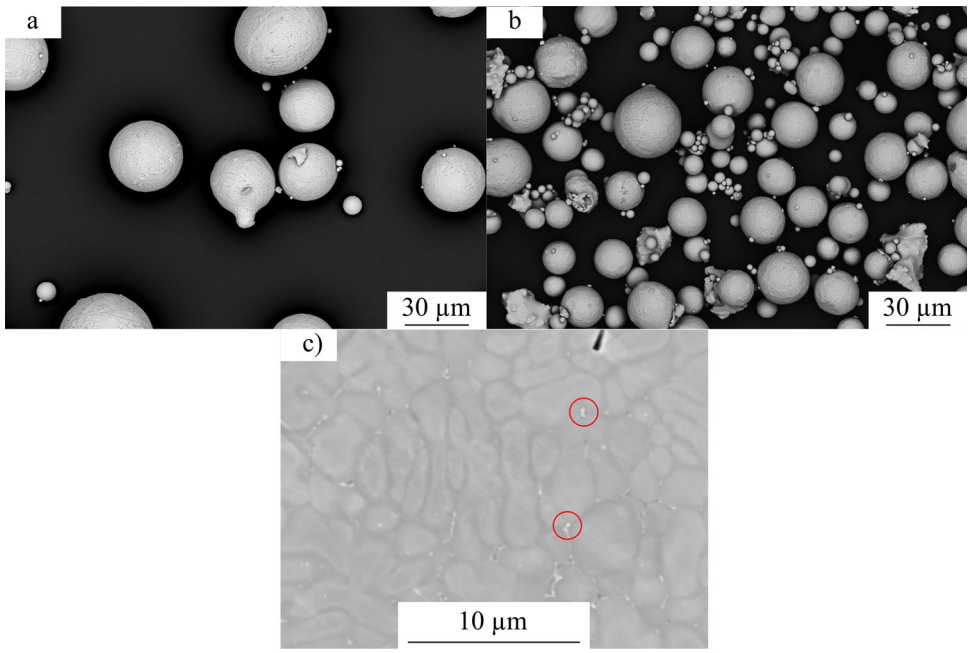

Fig. 1 BSE (backscattered electron) SEM image of the (a) coarse (25-45 µm), (b) fine powder (< 25 µm) and (c) cross-section of the coarse powder with bright phases marked by red circles

Table 2 Particle size distribution and oxygen content of the CMSX-4 powders

Powder	D_{10}, µm	D_{50}, µm	D_{90}, µm	Oxygen content ,wt.%
Coarse powder (25-45 µm)	14	41	61	0.019
Fine powder (< 25 µm)	9	18	29	0.036

Characterization Methods

The Accuraspray G3 System by Tecnar (Saint-Bruno-de-Montarville, Canada) measures particle temperatures and velocities. This system operates based on Two-Color Pyrometry, utilizing emitted energy at two different wavelengths to determine particle temperatures. For ascertaining particle velocities, the radiation emitted from the particles is detected by a two-slit mask with a known distance between the two measurement locations. The measurement of flight time between these two detectors enables the determination of particle velocities.

Metallographic cross sections were prepared to evaluate porosity, coating thickness and microstructure. After embedding and cutting, the samples were ground and polished using an ATM Saphir 550 (Struers GmbH, Germany). A scanning electron tabletop microscope Hitachi TM3000 (Hitachi High-Technologies Europe GmbH, Krefeld, Germany) was used for the microstructure observation (coating thickness and porosity). High-resolution images and energy dispersive spectroscopy (EDS) analyses were performed with the Gemini SEM 450 (Carl Zeiss AG, Oberkochen, Germany), equipped with an EDS detector ULTIM MAX 170 (Oxford Instruments, Abingdon, United Kingdom).

To analyze the single splat experiments, seven random SEM images of the sample surface on which splats were collected were taken at the same magnification. The total number of particles and molten splats in the image were then counted; only particles that are fully imaged in the image were counted. In addition, for the single splat samples of the coarse powder, only particles larger than 10 µm are counted. The diameter of the molten splats is analyzed on three randomly selected pictures. Image J was used to determine the porosity and the coating thickness. The coating thickness is determined by measuring the thickness at three different locations on three separate SEM images. Seven random SEM images were taken at 1000 x magnification to make a quantified statement about the porosity. The images are converted into binary images using the image analysis software, allowing the determination of the proportion of pores within the images.

An oxygen/nitrogen/hydrogen elemental analyzer LECO ON836 from LECO Corporation (St. Joseph, USA) was used to determine the oxygen content of the powder and the coatings.

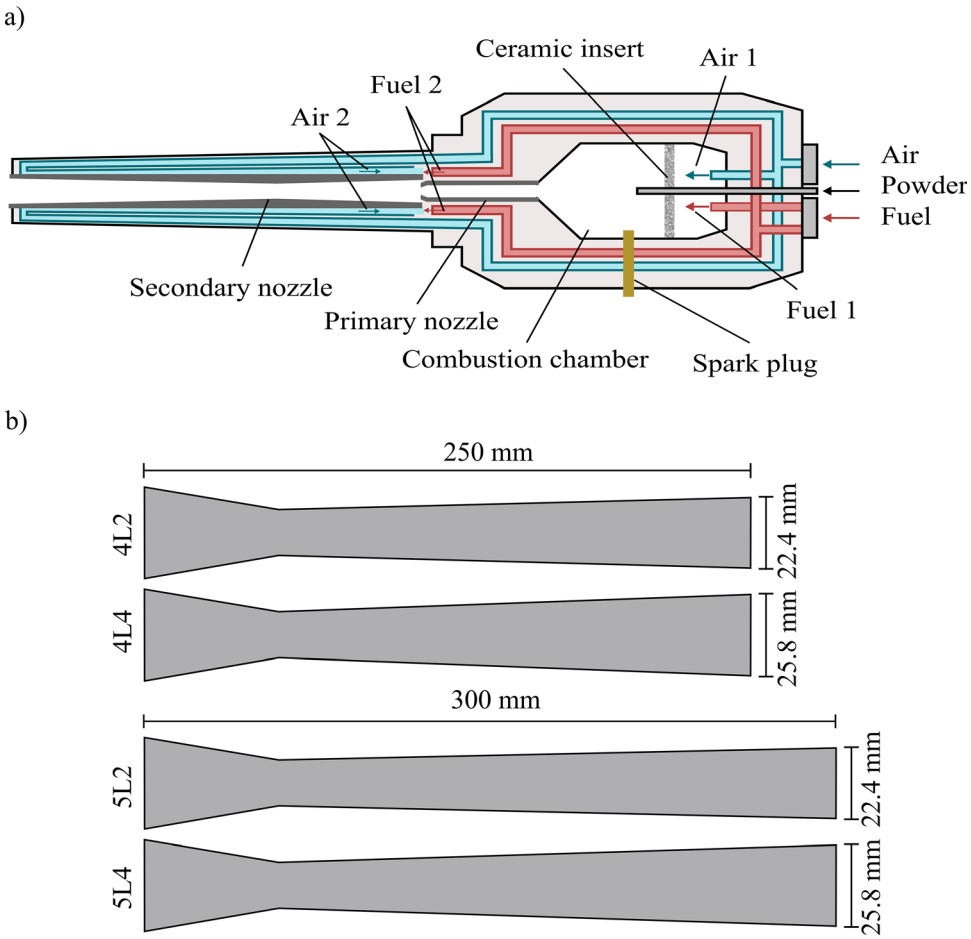

Fig. 2 (a) Sketch of the HVAF torch (according to (Ref 33)) showing powder and fuel injection locations and (b) different secondary nozzle geometries of the ceramic nozzles used for the experiments

Table 3 Test overview of the HVAF tests carried out to analyze the nozzle and powder influences (SS: single splat experiments)

Sample	Nozzle	Powder, μm	Air pressure, MPa	Fuel 1 pressure, MPa	Fuel 2 pressure, MPa
HVAF P1 /SS	4L2	< 25	0.74	0.69	0.72
HVAF P2	4L4	< 25	0.74	0.69	0.72
HVAF P3 /SS	5L2	< 25	0.77	0.69	0.72
HVAF P4	5L4	< 25	0.74	0.69	0.72
HVAF P5 /SS	4L2	< 25	0.81	0.72	0.79
HVAF P6	4L4	< 25	0.77	0.69	0.76
HVAF P7 /SS	5L2	< 25	0.78	0.72	0.79
HVAF P8	5L4	< 25	0.78	0.72	0.79
HVAF P9 /SS	4L2	25-45	0.74	0.69	0.72
HVAF P10	4L4	25-45	0.74	0.69	0.72
HVAF P11 /SS	5L2	25-45	0.77	0.69	0.72
HVAF P12	5L4	25-45	0.74	0.69	0.72
HVAF P13 /SS	4L2	25-45	0.81	0.72	0.79
HVAF P14	4L4	25-45	0.77	0.69	0.76
HVAF P15 /SS	5L2	25-45	0.78	0.72	0.79
HVAF P16	5L4	25-45	0.78	0.72	0.79

Table 4 Test overview of the HVAF tests carried out to investigate the influence of process parameters

Sample	Spray distance, mm	Surface speed, m min^{-1}	Powder feed rate in g min^{-1}	Carrier gas flow, L min^{-1}	Cycles
HVAF P17	300	100	100	45	16
HVAF P18	150	100	100	45	16
HVAF P19	200	100	100	45	16
HVAF P20	250	100	100	45	16
HVAF P21	350	100	100	45	16
HVAF P22	400	100	100	45	16
HVAF P23	450	100	100	45	16
HVAF P24	300	100	100	30	16
HVAF P25	300	100	100	60	16
HVAF P26	300	100	50	45	32
HVAF P27	300	100	150	45	11
HVAF P28	300	100	200	45	8
HVAF P29	300	25	100	45	4
HVAF P30	300	50	100	45	8
HVAF P31	300	75	100	45	12
HVAF P32	300	125	100	45	20
HVAF P33	300	150	100	45	24

Results and Discussion

Influence of Nozzle Configuration and Particle Size

Accuraspray Measurements: Particle Temperature and Velocity

In Fig. 3, particle temperatures and velocities measured for different nozzles are given, both for the fine and the coarse powder. The different pressure settings are also considered. If the coarse powder is used in combination with the 4L4 nozzle, no measurement could be made. This is likely due to the particle temperature being too low, leading to particles not being detected. It is important to highlight that the measurements obtained from the Accuraspray represent an averaged value of an ensemble of particles and do not offer insights into the distribution of particle velocities and temperatures. The Accuraspray system has a minimum

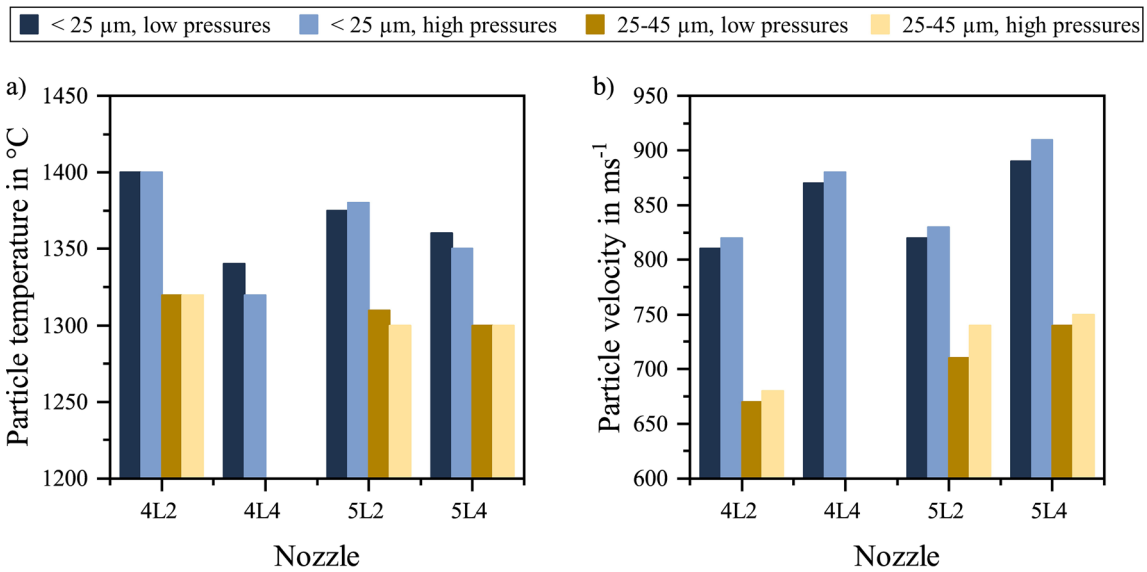

Fig. 3 Particle temperatures and velocities for the different secondary nozzles, measured at low and high pressures for the fine (< 25 µm) and the coarse powder (25-45 µm) using Accuraspray

detection capability for particle temperatures of around 1000 °C, primarily constrained by the limited thermal radiation emitted by cold particles. In general, the particle temperatures (Fig. 3a) are lower for the coarse powder than for the fine powder in all cases. It can be assumed that the time in the nozzle is not sufficient to completely heat up the coarser particles, despite the presumably longer dwell time due to the higher mass of the particles and therefore lower velocities. The higher inertia is also evident through the lower particle velocities compared to the fine powder. As stated before, the temperatures are probably lower, especially for the coarse powder, as a large proportion of the particles were likely not detected due to low temperatures. With a minor elevation in pressures, a small increase in particle velocities (Fig. 3b) becomes recognizable across all nozzles for both powders. This phenomenon arises from the increase of gas flow attributed to the application of higher pressures. Due to slightly shorter residence times in the nozzle, the particle temperature either experiences a slight decrease or remains constant. Only with the 5L2 nozzle in combination with the fine powder, a marginal temperature increase is observed. However, it is worth noting that this might be attributable to measurement inaccuracies, as the temperature differences under altered pressures are generally quite small.

The following results can be observed for the fine and the coarse powder. If the nozzle outlet diameter increases, i.e., the expansion ratio increases (from 1.39 to 1.84), the particle velocity increases and the particle temperature decreases slightly (4L2 to 4L4, 5L2 to 5L4). For example, the particle speed of the fine powder sprayed at low pressure settings increases from 810 to 870 m/s if sprayed with the 4L4 nozzle instead of the 4L2 nozzle. The temperature, on the other hand, drops by 60 °C. The reason for this is that fluids are compressible above a mach number of 0.3. If the diameter is increased, the fluid density decreases. To maintain the mass flow, the gas velocity increases with a simultaneous decrease in temperature. As a result, the particles also experience a higher acceleration, with a simultaneous reduction in temperature.

If the nozzle is extended, i.e., changed from 4L2 to 5L2 or from 4L4 to 5L4, the particle velocity increases slightly by 10 to 20 m/s. Since the nozzles 5L2 and 5L4 are 50 mm longer, the particles have a longer dwell time in the nozzle, which causes them to accelerate further. However, these changes are only very minor. The particle temperature increases when comparing the 4L4 nozzle with the 5L4 nozzle. However, a lower particle temperature can be observed if we use the 4L2 and the 5L2 nozzle. The particle temperatures for the coarse powder differ only slightly. As already mentioned, the residence time in the nozzle is probably not sufficient for heating the particles, which might cause some detection problems for the Accuraspray system. Two competing effects can likely be attributed to the particle temperature for the fine powder. For instance, the particles have a longer dwell time in the nozzle due to the longer nozzle, which leads to an increased particle temperature. At the same time, however, this also increases the particle velocity, which in turn leads to a reduction in temperature. The observation that particle temperature decreases when switching from the 4L2 to the 5L2 nozzle for fine powders but increases when switching from the 4L4 to the 5L4 nozzle, may also be due to differences in gas stoichiometry, which likely vary across these nozzles. Each nozzle operates under specific pressure conditions to ensure flame stability, resulting in slight pressure adjustments between nozzle types. Furthermore, Mauer et al. (Ref 34) demonstrated that even when identical pressures are applied, the mass flow rates vary between these nozzles, further influencing particle temperature behavior.

Single Splat Trials

The results described in the previous chapter can also be confirmed by the single splat experiments. Top views of the single splat samples for the fine powder at low pressure settings are given in Fig. 4. By looking at the single splat samples, it is possible to determine the state of the particles when they hit the substrate. Thus, it can be distinguished whether the particles were molten (Fig. 4 1 & 2), partially molten (Fig. 4 3 & 4), or softened (Fig. 4 5 & 6) during flight.

In order to make a quantified statement, seven images of random positions were taken, and the molten particles and the total number of particles were counted (Table 5). However, it should be noted that precise quantification is a challenge. For example, particles can overlap in the center of the spray track's plume center area, which means that the counting is always performed in an area where it is possible to identify individual splats/particles. Due to the varying spray plume diameter depending on the nozzle configuration, it cannot be ruled out that the observed areas also have some associated uncertainty. It can be assumed that the number of molten particles decreases from the center of the spray track. In addition, it is sometimes difficult to distinguish individual splashes, making it hard to tell in some places whether a particular observation is a splash or a broken particle. Moreover, it was subsequently established that the spray gun was defective during the tests with high pressures, which is why a discussion of this would not be meaningful. For this reason, only the tests at low pressures are described below.

For both the fine and the coarse powder, nozzles 4L2 and 5L2, where the highest particle temperatures were measured, have the largest number of completely molten

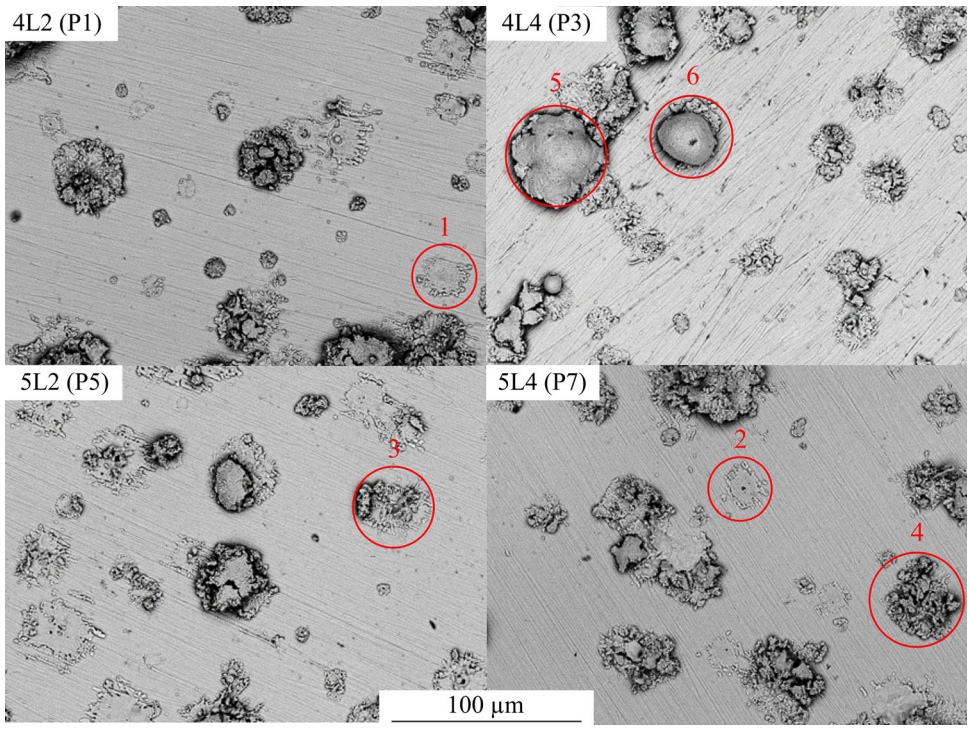

Fig. 4 BSE-images of the single splat tests of the fine powder for the different nozzles; 1 & 2 molten particles, 3 & 4 semi-molten particles, 5 & 6 softened particles

Table 5 Evaluation of the absolute and percentage of molten particles for the fine (< 25 µm) and coarse (25 − 45 µm) powder when using the different secondary nozzles at low pressures

Nozzle	Powder, µm	Number of molten particles	Molten particles, %	Total number of particles
4L2	< 25	61	37	165
4L4	< 25	5	3	149
5L2	< 25	69	42	165
5L4	< 25	24	21	117
4L2	25-45	19	49	39
4L4	25-45	4	15	27
5L2	25-45	14	40	35
5L4	25-45	7	21	34

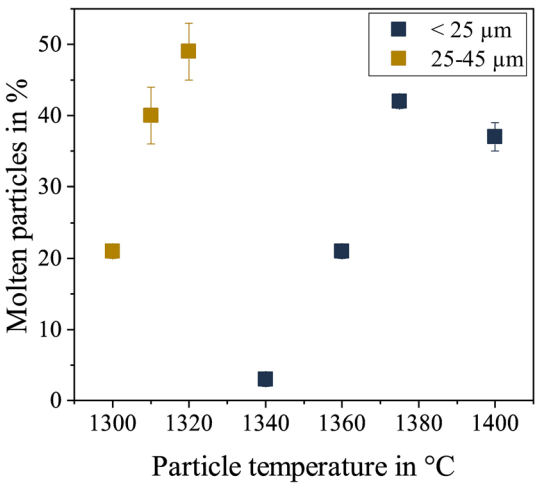

Fig. 5 Percentage of molten particles as a function of particle temperature

particles, both in absolute and percentage terms (see Fig. 5). For the 4L4 nozzle, for which the lowest particle temperature was measured, the lowest proportion of molten particles was found on the sample surface. The total number of particles on the samples coated with nozzles 4L2 and 5L2 is the highest. This is probably attributed to the fact that the particles adhere better to the substrate due to the increased temperature. For the coarse powder, on the other hand, there are only marginal differences, but with a similar trend. In general, it is noticeable that there are significantly fewer particles on the surfaces of the substrates for the coarse powder.

This effect can possibly be attributed to the lower temperatures of the particles, which makes them less soft and causes them to bounce off the surface. The same feed rate was used for both the fine and the coarse powder, however as the particles in the coarse powder are larger and, therefore, heavier, comparatively fewer particles are

deposited. As a result, the percentage of molten particles is actually similar to that of the fine powder (see Fig. 5).

It can be seen that the melted splats are mostly smaller particles, as the smaller mass can be heated up more quickly. The smaller diameter of the splats can confirm this. The largest molten splat of all analyzed samples has a diameter of approx. 45 µm and was found on the sample sprayed with the 4L2 nozzle in combination with the fine powder and the 5L2 nozzle when using the coarse powder. The fact that the same maximum melted particle size was found for both powder fractions can be explained by the overlap between the fractions, resulting in a certain proportion of particles having the same size. This size appears to be within the range of the maximum meltable mass. The flattening during particle impact further increases this diameter compared to the original particle diameter. The diameter of the merely softened particles, in comparison, probably changes less. However, bigger splats are more likely to be found in the center area of the spray track, as it can be assumed that the temperatures in this area of the flame are higher, and, therefore, larger particles can also be molten. The nozzles that achieved the highest particle temperatures (4L2 and 5L2) show the highest number of molten particles (Fig. 6), as well as the highest splat sizes for both the fine and coarse powders. Due to the higher temperatures, larger particles can be completely melted. The 4L4 nozzle, which achieved the lowest particle temperatures, only has splats up to 30 µm in size, and therefore achieved smaller splat sizes than the other nozzles. In general, it can be seen that the fine powder contains the majority of completely molten particles with smaller diameters than the coarse powder. This can be explained by the particle size distributions. The fact that relatively small molten splats are also found in the coarse powder is probably due to the fact that the powder contains a small proportion of fine powder. In addition, the SEM images of the initial powder showed that a large number of small satellite particles adhered to the coarse particles. These can presumably be molten during the process.

Coating Thickness, Porosity and Oxygen Content

Figure 7 shows an example of two coatings produced with the 5L4 nozzle. The dashed lines in the lower part of the image indicate the interface between substrate and coating. With the fine powder, dense coatings can be produced (Fig. 7a). If the coarse powder is used, only a coating with a strongly fluctuating coating thickness can be fabricated (Fig. 7b). It can be seen that many horizontal cracks run through the coating with the coarse powder, and the bonding between the particles seems to be low. It can be assumed that the brittle powder material is not sufficiently heated. Therefore, the particle deformation is difficult. In combination with the high velocity, the particles break or bounce back. The poorer layer quality in the case of coarse powder can be linked to the characteristics of the splat experiments. Coarse powder generally resulted in fewer particles on the surface, although the same feed rate may also influence this outcome. Additionally, there is a higher occurrence of rebound craters and particles that are only slightly softened, retaining nearly their original round shape, compared to fine powder.

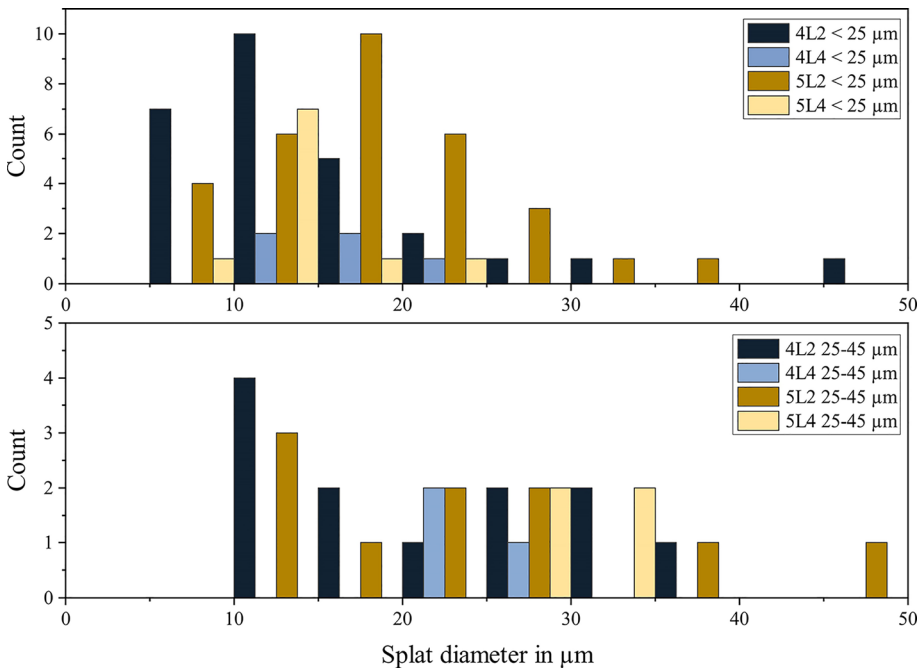

Fig. 6 Number of molten splats sorted by splat diameter for the fine (< 25 µm) and coarse (25-45 µm) powder in combination with the different nozzles

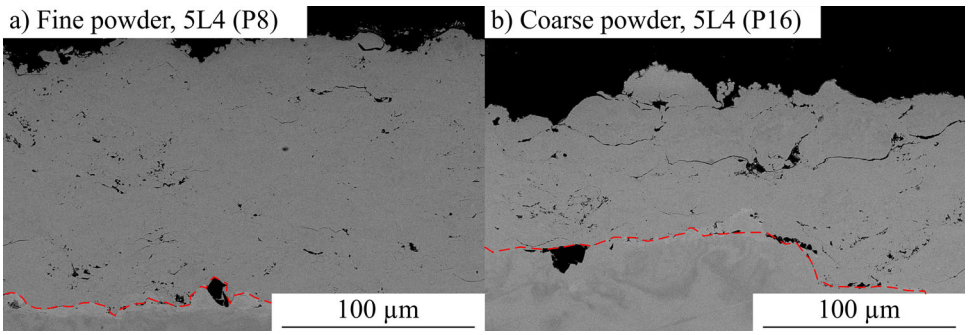

Fig. 7 BSE SEM image of the coatings produced with the 5L4 nozzle: (a) fine powder (< 25 µm) and (b) coarse powder (25-45 µm)

The coating thicknesses sprayed with different secondary nozzle configurations are shown in Fig. 8a). It can be seen that the 4L4 nozzle produces the lowest and the 4L2 nozzle the highest coating thickness. This applies to both the fine and the coarse powder and also for both pressure settings. Even if most of the error bars overlap and no clear statements can be made, the same trend can be observed for both powders and pressure settings. It can therefore be assumed that there are differences in the coating thickness when using the different nozzles.

A correlation between particle temperature and coating thickness has been found (Fig. 8b)). The coating thickness of the samples increases as the particle temperature rises. Therefore, the finer powder leads to higher coating thicknesses and thus higher deposition efficiencies (Table 6) than the coarse powder. The reason for this is that more molten/softened material sticks to the surface, as it can be seen from the single splat experiments, if the particle temperature is higher. The effect of temperature is more pronounced due to the low ductility of the material. If the material is not sufficiently softened by higher temperatures, it will break during impact, and some of the material will bounce back. When examining the data of the fine powder under various pressure settings at 1400 °C, it is noticeable that higher pressure configurations result in a thinner coating. It is conceivable that particle velocity also influences the coating thickness. The elevated pressure settings lead to slightly increased impact velocities, potentially causing more portions of the powder to break or bounce back from the substrate. Additionally, inaccuracies in temperature measurements could also contribute to a distortion of the results.

If one compares the porosity (Fig. 9) of the samples that were produced with different nozzles, a dependence on the particle velocity is visible. At higher particle velocities, the coatings have a lower porosity than at slower velocities. Thus, the lowest porosity for both powders is observed with the 5L4 nozzle and the highest with the 4L2 nozzle. The reason for this is presumably that the higher kinetic energy leads to a better deformation of the particles which leads to reduced porosity in the coating. This is also demonstrated in the single-splat experiments, where, for

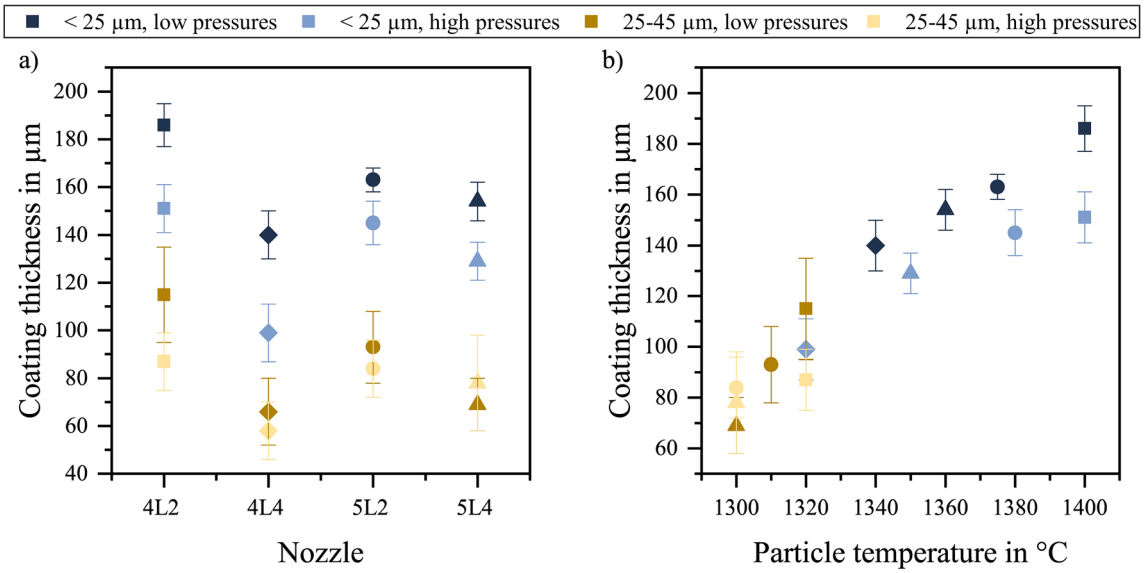

Fig. 8 (a) Coating thickness for the different secondary nozzles, measured at low and high pressures for the fine (< 25 µm) and the coarse powder (25-45 µm) and (b) Coating thickness as a function of the particle temperature

Table 6 Deposition efficiency of the experiments investigating the nozzle and powder influences

Sample	Nozzle	Powder, µm	Pressure settings	Deposition efficiency, %
HVAF P1	4L2	< 25	low	58
HVAF P2	4L4	< 25	low	38
HVAF P3	5L2	< 25	low	43
HVAF P4	5L4	< 25	low	39
HVAF P5	4L2	< 25	high	42
HVAF P6	4L4	< 25	high	30
HVAF P7	5L2	< 25	high	40
HVAF P8	5L4	< 25	high	36
HVAF P9	4L2	25-45	low	26
HVAF P10	4L4	25-45	low	17
HVAF P11	5L2	25-45	low	25
HVAF P12	5L4	25-45	low	19
HVAF P13	4L2	25-45	high	22
HVAF P14	4L4	25-45	high	15
HVAF P15	5L2	25-45	high	20
HVAF P16	5L4	25-45	high	20

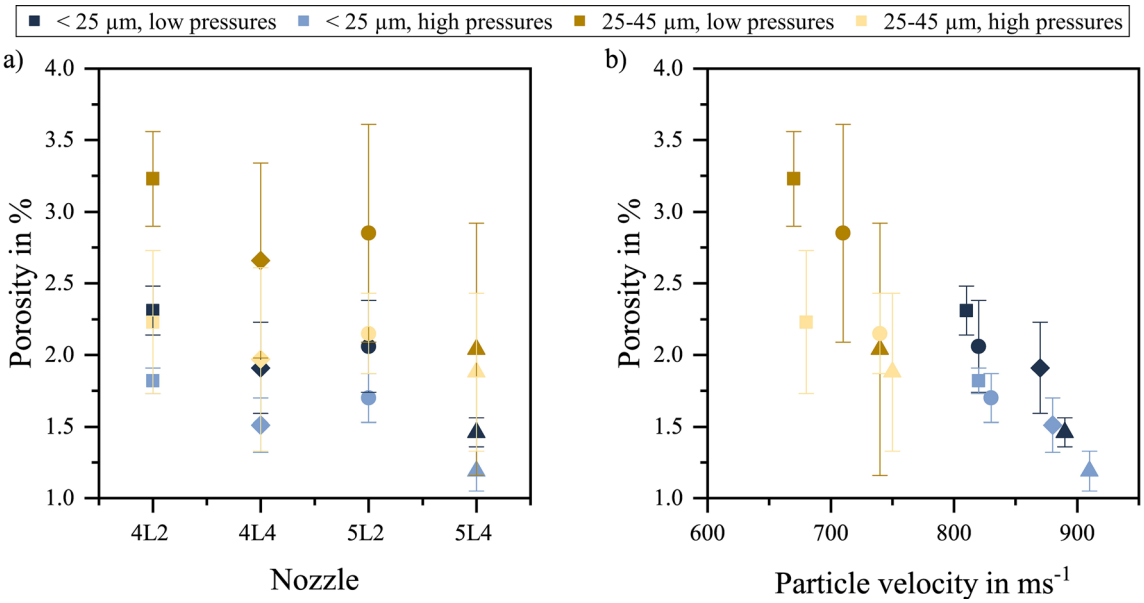

Fig. 9 (a) Coating porosity for the different secondary nozzles, measured at low and high pressures for the fine (< 25 µm) and the coarse powder (25-45 µm) and (b) Coating porosity as a function of the particle velocity

example, coarser particles were less deformed due to being colder and slower. A higher porosity is generally observed for the coarser powder than for the fine powder. However, it should be mentioned that porosity also includes poor bonds and cracks, which influences the measurement.

Figure 10 shows the oxygen values of the coatings. It should be noted that only two measurements were carried out for the 4L4 nozzle instead of the usual three. No measurement data is available for the coarse powder, as it was not possible to separate the material from the substrate. As before, the differences in the values are relatively small. However, it can be seen that oxygen is taken up during spraying, as the oxygen content in the initial powder is 0.112-0.224 wt.% lower than in the coatings (compare with Table 2). The highest oxygen values are observed in case of the 4L2 and 5L2 nozzles. Using a nozzle in combination with different pressure settings does not have a significant influence. Probably because the temperature differences are minimal when a nozzle is operated with different pressure settings. If the oxygen values are related to the measured particle temperatures, it can be seen that the oxygen content slightly increases with increasing temperatures. This is

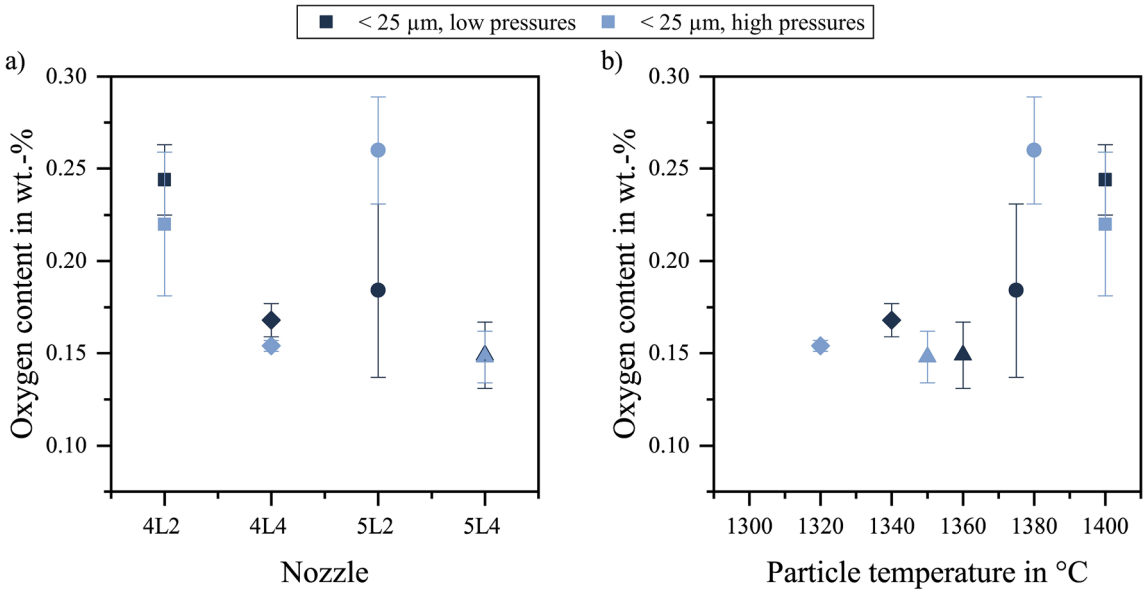

Fig. 10 (a) Oxygen content for the different secondary nozzles, measured at low and high pressures for the fine powder (< 25 µm) and (b) Coating porosity as a function of the particle velocity

due to the increased reactivity of the elements at higher temperatures.

For the further investigations of the influence of process parameters, only the finer powder was used, as it had both higher deposition efficiencies and lower porosities. The lowest porosity and the lowest oxygen content can be achieved with the 5L4 nozzle while maintaining a reasonable layer thickness. In this case, porosity and oxygen content are given higher priority than layer thickness, as these are advantageous for the planned heat treatments.

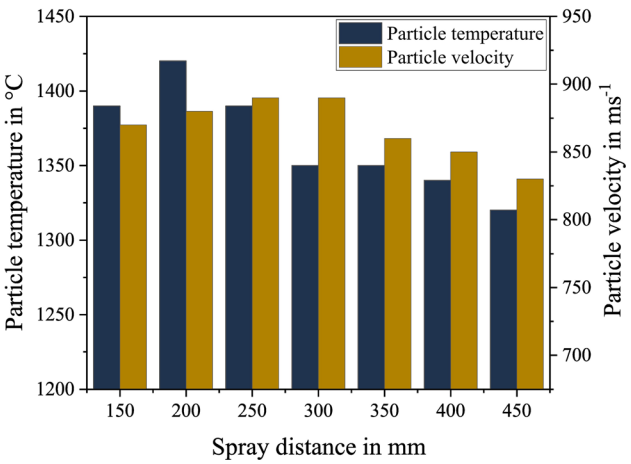

Fig. 11 Particle temperatures and velocities as a function of spray distance measured by Accuraspray

Influence of the Spray Distance

The particle temperatures and velocities measured by Accuraspray as a function of the spray distance can be found in Fig. 11.

Both velocity and temperature increase slightly at first, as the particle temperature and velocity have probably not yet reached the values of the processing gas when leaving the nozzle. The maximum particle temperature is reached at a spray distance of 200 mm, and the maximum particle velocity after 250 mm. Afterward, both particle velocity and temperature decrease, due to the reduced temperature and velocity of the process gas. This also explains the decrease in coating thicknesses with increasing the spray distance (Fig. 12a). The coating thickness remains relatively constant up to 300 mm spray distance, then decreases with increasing spray distance. The same trend is observed for the deposition efficiency, which decreases from 36% at a spray distance of 300 mm to 16% at a distance of 450 mm. As explained before, the decreasing thickness is probably related to the simultaneously decreasing particle temperatures and velocities.

Figure 12(b) shows that the oxygen content in the coatings initially reduces as the spraying distance increases, presumably because both the particle and ambient temperatures decrease. From a spraying distance of 350 mm on, the oxygen content in the coatings increases again. This could be due to the increased porosity in the coatings and the longer in-flight time.

The porosity first decreases at a spray distance of 150 to 300 mm and then increases again, reaching a value of 2.4%

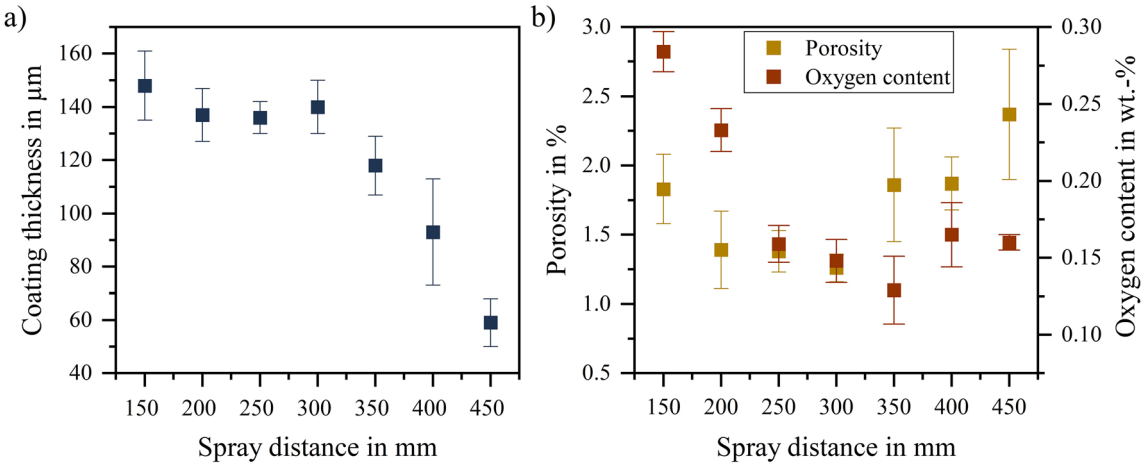

Fig. 12 (a) Coating thickness as a function of the spray distance and (b) porosity and oxygen content as a function of the spray distance

at 450 mm. At 1.2%, the porosity reaches the lowest value at a distance of 300 mm. It should be mentioned that the standard deviation of the measurements of the individual samples is quite large. Despite this, a trend can be seen in the porosity measurements, which correlates with the measured particle velocities. The initially decreasing porosity (up to 300 mm spray distance) with increasing spraying distance can be explained by the slightly increasing particle velocity, which causes the particles to be more deformed on impact. The porosity values increase when the particle velocities decrease again from a spraying distance of 300 mm. The additional slightly higher temperature could also have an influence. This softens the particles more and facilitates deformation.

Influence of the Powder Feed Rate

The particle temperatures and velocities measured by Accuraspray as a function of the powder feed rate can be found in Fig. 13. Both the particle velocity and the particle temperature remain largely constant. These results are also reflected in the coatings produced. The coating thickness, oxygen content and porosity are given in Fig. 14. It can be seen that the powder feed rate has no major influence on these values.

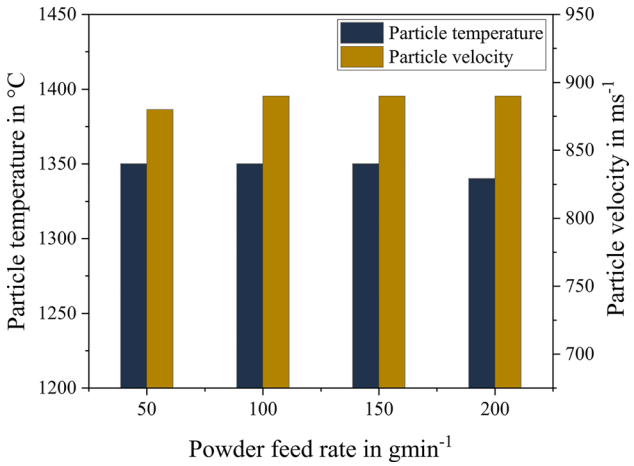

Fig. 13 Particle temperatures and velocities measured as a function of the powder feed rate using Accuraspray

Influence of the Carrier Gas Flow

If the carrier gas flow is changed, no major differences in particle temperature and velocity can be detected with the Accuraspray system (Fig. 15). Figure 16 shows that also the characteristic values of the coatings remain almost constant as the carrier gas flow changes.

Influence of the Surface Speed

In Fig. 17 the influence of surface speed on coating thickness, oxygen content and porosity is shown. The coating thickness does not appear to be dependent on the sur- face speed. Porosity shows a marginally increase with velocity above 100 m/min. With reduced velocities the local substrate temperature increases, which causes the particles to experience higher temperatures during impact and the solidification to proceed more slowly, which in turn leads to a lower porosity.

Microstructure

The microstructures of the different coatings produced with the fine powder are similar, so a sample produced with the parameters of sample HVAF P8 (Fig. 18) is analyzed in detail as an example.

In some cases, individual splats can be identified in the coating. For example, two particles are marked by red dashed lines in Fig. 18a. The larger particles, which are less

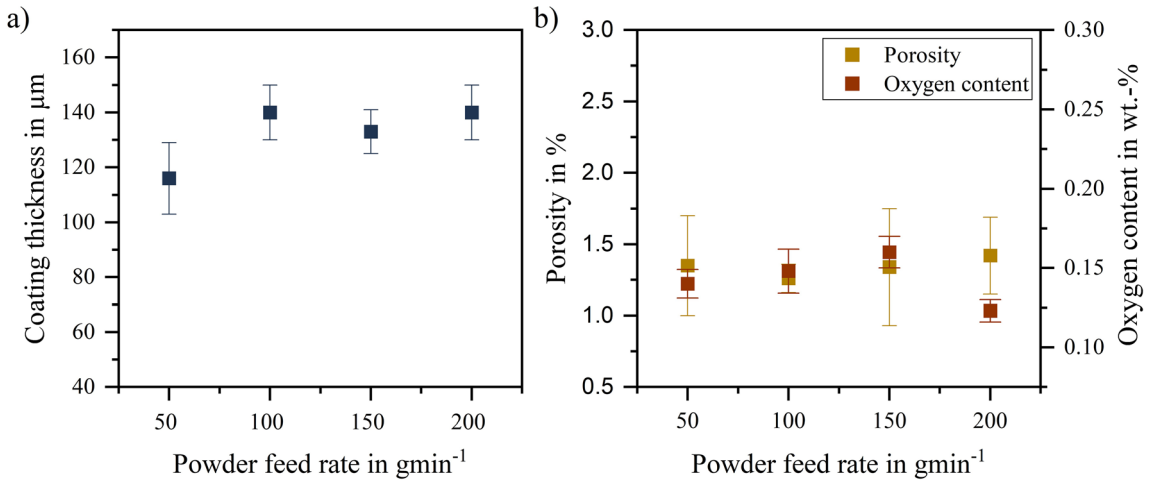

Fig. 14 (a) Coating thickness as a function of the powder feed rate and (b) porosity and oxygen content as a function of the powder feed rate

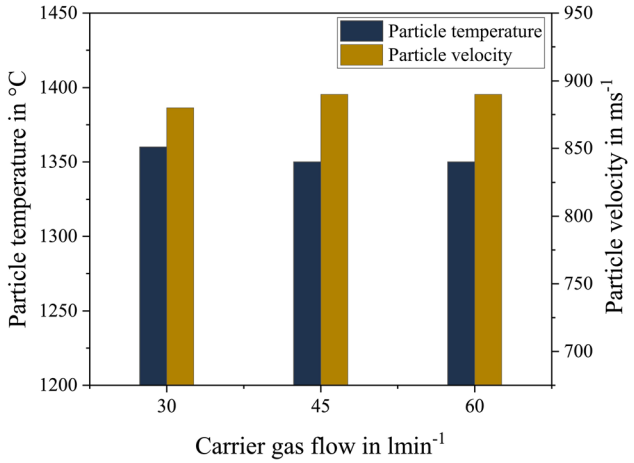

Fig. 15 Particle temperatures and velocities measured as a function of the carrier gas flow using Accuraspray

deformed due to the lower temperatures, are particularly easy to recognize. The splats of the smaller, completely molten, or heavily deformed particles are difficult to identify individually. The initial dendritic structure of the powder used is still clearly recognizable in the coarser particles. In addition, bright phases (see Fig. 18b), which are already present in the initial powder, can be recognized in these particles. These precipitates are probably TCP phases of the material, which appear bright in the SEM due to the higher atomic number. These phases cannot be found in the areas consisting of more deformed, molten particles. It is assumed that the TCP phases are dissolved due to the high temperatures reached by the particles and are no longer precipitated due to the rapid cooling on impact with the substrate. Pores and oxide films can be found between the individual splats. The quantity varies depending on the nozzle configurations, powder and process parameters used, as discussed in the previous chapters. Fig. 18b) shows the areas where EDS measurements were carried out. As

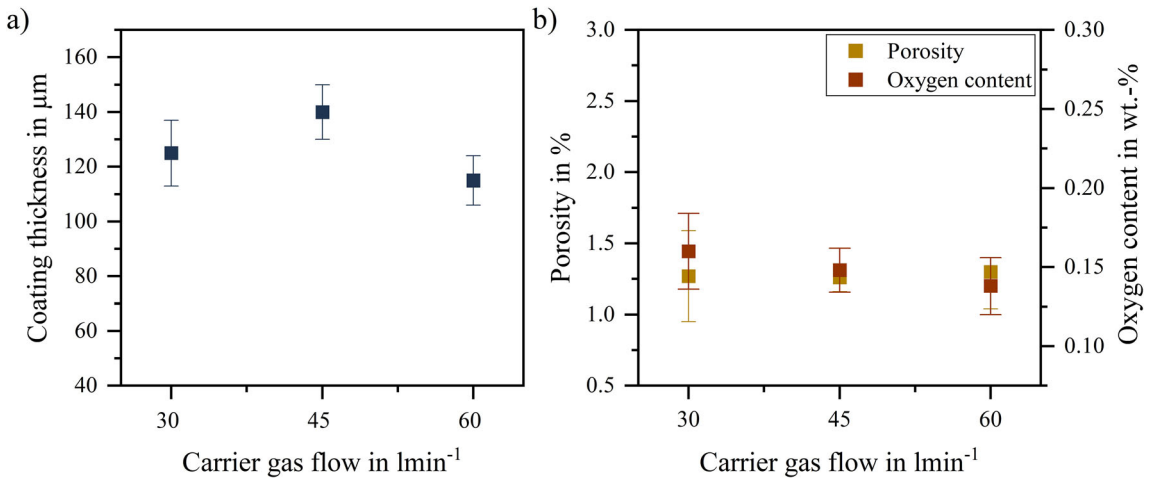

Fig. 16 (a) Coating thickness as a function of the carrier gas flow and (b) porosity and oxygen content as a function of the carrier gas flow

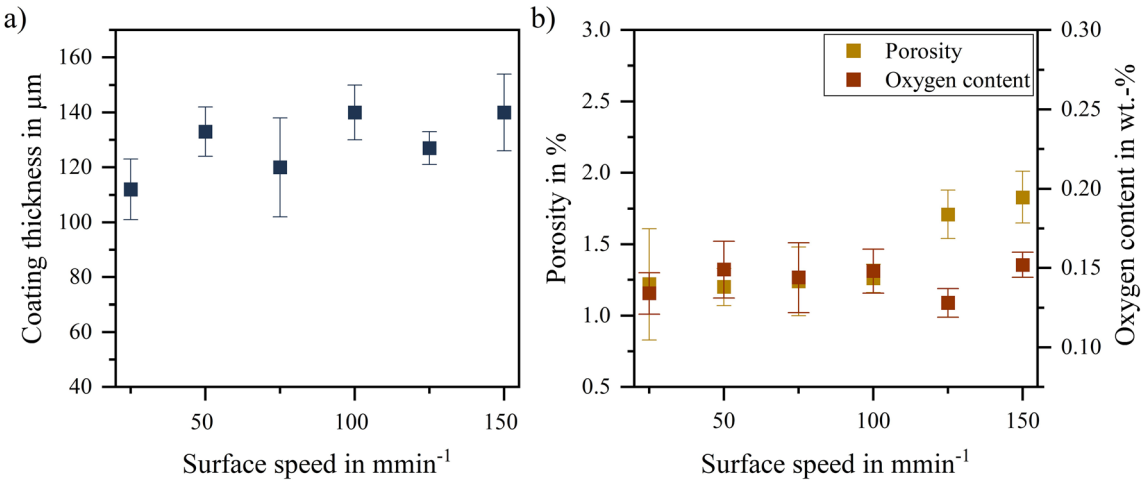

Fig. 17 (a) Coating thickness as a function of the surface speed and (b) porosity and oxygen content as a function of the surface speed

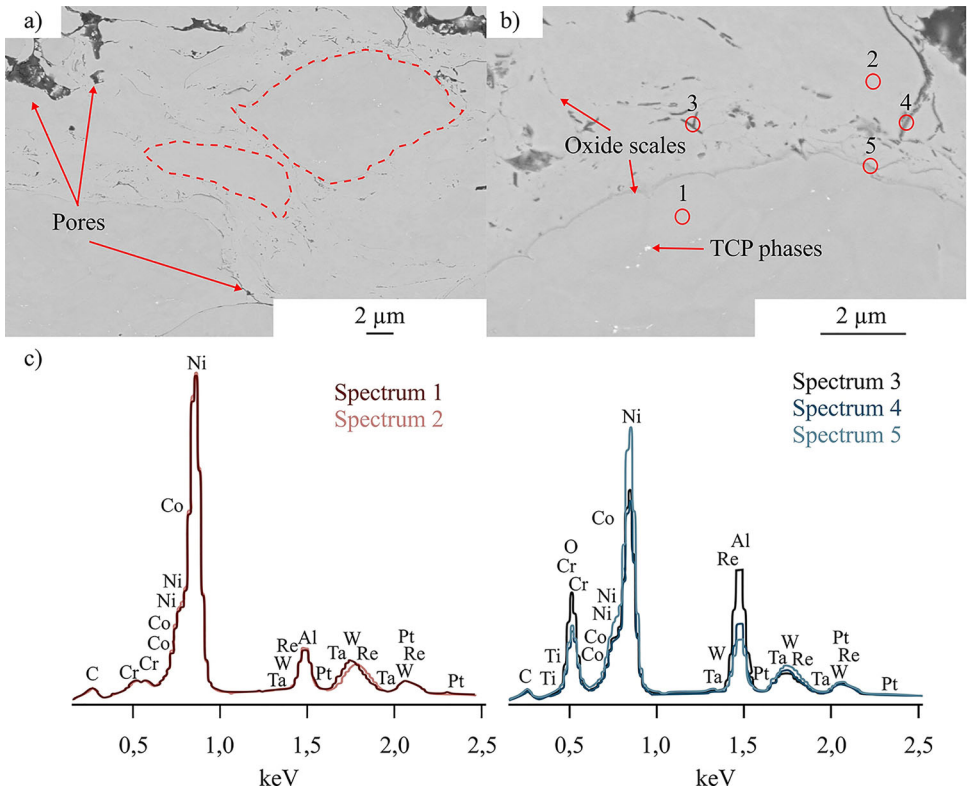

Fig. 18 (a) BSE SEM image of the microstructure taken in the middle of the coating from sample P8, the dashed red lines indicate single particles, (b) BSE-SEM image with the positions of the EDS measuring points, (c) corresponding EDS spectra

the interaction volume of the electron beam with the material is much larger than the analyzed particles, a quantitative analysis makes no sense. Nevertheless, in the darker areas, increased oxygen and aluminum values can be detected (Fig. 18c)), which makes perfect sense as oxides would appear darker in the BSE images due to the lower average atomic number. It is assumed that an in-flight oxidation of the particles takes place. In addition, oxidation of the substrate surface or the coating surface may also occur.

Figure 19 shows an EBSD image of the coating. The dark regions are likely nanocrystalline grains situated along splat surfaces and interfaces, too small to be resolved by the EBSD detector due to their size falling below its step size and resolution limits. These fine microstructures likely form due to the rapid cooling of molten and partially molten particles as they solidify on contact with the substrate or the previously deposited coating layer. Occasionally, larger grains can be observed, which are likely particle regions that did not fully melt and only underwent

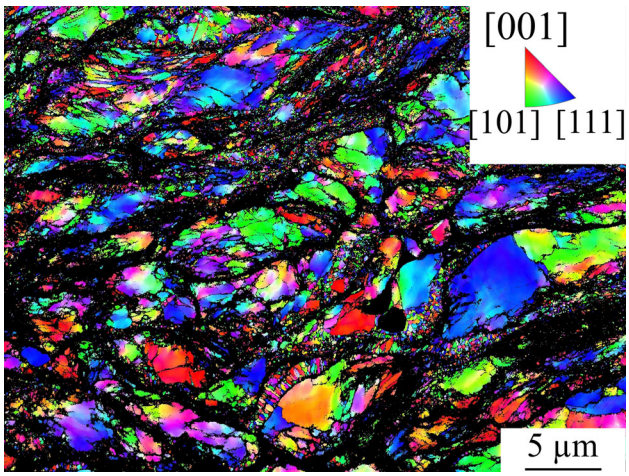

Fig. 19 EBSD inverse pole figure map of sample P8

deformation. Overall, a very fine grain structure is evident throughout the entire coating layer. The image shows a pronounced variation in the crystallographic orientation of individual grains, which is clearly visible through the different colors in the orientation mapping.

Summary and Conclusions

In the present study, high velocity air spraying (HVAF) was investigated as a possible repair technique for single crystal nickel-based superalloys. The following conclusions can be drawn from these results:

- Polycrystalline nickel-based superalloy repair coatings can be successfully produced using the HVAF process. This can be seen as the first step toward single-crystal repair.
- Different secondary nozzles lead to different particle temperatures and particle velocities, which in turn have an influence on the resulting microstructure of the coating. The lowest porosity was achieved by using the nozzle with the highest particle velocity. However, the influence of the different nozzles on the porosity is very small. The resulting coating thickness is highest with the 4L2 nozzle. This nozzle also exhibits the highest temperature. Nevertheless, the differences in coating thickness among the various nozzles are relatively small. The oxygen content also increases with higher particle temperatures.
- The finer powder enables higher coating thicknesses and lower porosities to be achieved. When using the coarse powder, the particles are not heated sufficiently. As the material is brittle at low temperatures, this leads to inadequate and inhomogeneous coating formation.
- Higher pressure settings result in increased particle velocities and a slight increased or constant particle temperature. Porosity and coating thickness decrease under higher pressures, likely due to the elevated particle velocities at nearly constant temperatures, leading to a higher deformation of the particles but potentially also resulting in more material splattering.
- The influence of different spray parameters such as spray distance, powder feed rate, carrier gas flow and surface speed were investigated. Only the spray distance has a significant influence on the coating properties. With increasing spray distance, the particle temperature and velocity decrease, which leads to a reduction in coating thickness and oxygen content. An increase in porosity is observed.
- The final parameters selected for the production of further coatings are the 5L4 nozzle in combination with high pressure settings and fine powder, a spray distance of 300 mm, a surface speed of 100 m/min, a carrier gas flow of 45 L/min, and a powder feed rate of 100 g/min, as these parameters yield both low porosity and low oxygen content.

Acknowledgments The present work was funded within the project T5 in SFB/TR 103 “From Atoms to Turbine Blades” by the German research Foundation (DFG), project nr. 190389738. We would like to thank our cooperation partners for providing the single crystal superalloy and powder.

Funding Open Access funding enabled and organized by Projekt DEAL.

References

1. R.C. Reed, *The Superalloys: Fundamentals and Applications*, Cambridge University Press, Cambridge, 2006.

2. D. Goldschmidt, Einkristalline Gasturbinenschaufeln aus Nickelbasis-Legierungen. Teil I: Herstellung und Mikrogefüge (Single-Crystal Gas Turbine Blades Made of Nickel-Based Alloys. Part I: Manufacture and Microstructure), *Mat. wiss. u. Werkstofftech*, 1994, **25**, p 311-320.
3. S. Ackert, Basics of Aircraft Maintenance Reserve Development and Management, Aircraft Monit., 2012.
4. K. C. Antony and G. W. Goward, Aircraft Gas Turbine Blade and Vane Repair, *Superalloys 1988* (Sixth International Symposium), (1988).
5. B. A. Rottwinkel, Verfahrenstechnische Grundlagen für das epitaxiale Rissschweißen in einkristallinen Nickelbasis-Superlegierungen (*Process engineering fundamentals for epitaxial crack cladding in single-crystal nickel-based superalloys*), Ph.D. thesis, MyCoRe Community (2022). https://doi.org/10.21268/20221111-0.
6. B. Rottwinkel, A. Pereira, I. Alfred, C. Noelke, V. Wesling, and S. Kaierle, Turbine blade tip single crystalline clad deposition with applied remelting passes for well oriented volume extension, *J. Laser Appl.*, 2017 https://doi.org/10.2351/1.4983667
7. M. Gäumann, C. Bezencon, P. Canalis, and W. Kurz, Single-Crystal Laser Deposition of Superalloys: Processing–Microstructure Maps, *Acta mater*, 2001, **49**(6), p 1051-1062. https://doi.org/10.1016/S1359-6454(00)00367-0
8. M. Gäumann, S. Henry, and F. Cleton, Epitaxial Laser Metal Forming: Analysis of Microstructure Formation, *Mater. Sci. Eng., A*, 1999, **271**(1–2), p 232-241.
9. R. Vilar, A. Almeida, and E.C. Santos, Multilayer Laser-Assisted Deposition on Single Crystal Superalloy Substrates, *Int. J. Microstruct. Mater. Prop.*, 2013, **8**(1/2), p 4-16. https://doi.org/10.1504/IJMMP.2013.052642
10. R. Vilar and A. Almeida, Repair, and Manufacturing of Single Crystal Ni-Based Superalloys Components by Laser Powder Deposition—A Review, *J. Laser Appl.*, 2014 https://doi.org/10.2351/1.4862697
11. B. Rottwinkel, L. Schweitzer, C. Noelke, S. Kaierle, and V. Wesling, Challenges for Single-crystal (SX) Crack Cladding, *Phys. Procedia*, 2014, **56**, p 301-308. https://doi.org/10.1016/j.phpro.2014.08.175
12. B. Rottwinkel, C. Noelke, S. Kaierle, and V. Wesling, Crack Repair of Single Crystal Turbine Blades Using Laser Cladding, Technology, *Procedia CIRP*, 2014, **22**, p 263-267. https://doi.org/10.1016/j.procir.2014.06.151
13. S. Kaierle, L. Overmeyer, I. Alfred, B. Rottwinkel, J. Hermsdorf, V. Wesling, and N. Weidlich, Single-Crystal Turbine Blade Tip Repair by Laser Cladding and Remelting, *CIRP J. Manuf. Sci. Technol.*, 2017, **19**, p 196-199. https://doi.org/10.1016/j.cirpj.2017.04.001
14. A. Basak, R. Acharya, and S. Das, Additive Manufacturing of Single-Crystal Superalloy CMSX-4 Through Scanning Laser Epitaxy: Computational Modeling, Experimental Process Development, and Process Parameter Optimization, *Metall. Mater. Trans. A*, 2016, **47**, p 3845-3859. https://doi.org/10.1007/s11661-016-3571-y
15. Z. Chen, W. Li, L. Wang, X. Wei, and Z. Liu, Investigation on the hot Crack Sensitivity of a Nickel-Based Single Crystal Superalloy Fabricated by Epitaxial Laser Metal Forming, *J. Alloys Compd.*, 2023 https://doi.org/10.1016/j.jallcom.2022.167436
16. K. Ogawa and D. Seo, Repair of Turbine Blades Using Cold Spray Technique, *Advances in Gas Turbine Technology*. E. Benini Ed., IntechOpen, London, 2011, p 499–526. https://doi.org/10.5772/23623
17. Q. Blochet, F. Delloro, F. N'Guyen, D. Jeulin, F. Borit, and M. Jeandin, Effect of the Cold-Sprayed Aluminum Coating-Substrate Interface Morphology on Bond Strength for Aircraft Repair Application, *J. Therm. Spray Technol.*, 2017, **26**(4), p 671-686. https://doi.org/10.1007/s11666-017-0548-3
18. S. Yin, P. Cavaliere, B. Aldwell, R. Jenkins, H. Liao, W. Li, and R. Lupoi, Cold Spray Additive Manufacturing and Repair_ Fundamentals and Applications, *Addit. Manuf.*, 2018, **21**, p 628-650. https://doi.org/10.1016/j.addma.2018.04.017
19 J. Fiebig, E. Bakan, T. Kalfhaus, G. Mauer, O. Guillon, and R. Vaßen, Thermal Spray Processes for the Repair of Gas Turbine Components, *Adv. Eng. Mater*, 2020 https://doi.org/10.1002/adem.201901237
20 T. Kalfhaus, M. Schneider, B. Ruttert, D. Sebold, T. Hammerschmidt, J. Frenzel, R. Drautz, W. Theisen, G. Eggeler, O. Guillon, and R. Vaßen, Repair of Ni-Based Single-Crystal Superalloys Using Vacuum Plasma Spray, *Mater. Design*, 2019 https://doi.org/10.1016/j.matdes.2019.107656
21. T. Kalfhaus, H. Schaar, F. Thaler, B. Ruttert, D. Sebold, J. Frenzel, I. Steinbach, W. Theisen, O. Guillon, T.W. Clyne, and R. Vaßen, Path to Single-Crystalline Repair and Manufacture of Ni-Based Superalloy Using Directional Annealing, *Surface & Coatings Technology*, 2021 https://doi.org/10.1016/j.surfcoat.2020.126494
22. V. Matikainen, H. Koivuluoto, P. Vuoristo, J. Schubert, and Š Houdková, Effect of Nozzle Geometry on the Microstructure and Properties of HVAF-Sprayed WC-10Co_4Cr and Cr_3C_2-25NiCr Coatings, *J. Therm. Spray Technol.*, 2018, **27**, p 680–694. https://doi.org/10.1007/s11666-018-0717-z
23. A. Vardelle, C. Moreau, J. Akedo, H. Ashrafizadeh, C.C. Berndt, J. Oberste Berghaus, M. Boulos, J. Brogan, A.C. Bourtsalas, A. Dolatabadi, M. Dorfman, T.J. Eden, P. Fauchais, G. Fisher, F. Gaertner, M. Gindrat, R. Henne, M. Hyland, E. Irissou, E.H. Jordan, K. Aik Khor, A. Killinger, Y. Lau, C. Li, L. Li, J. Longtin, N. Markocsan, P.J. Masset, J. Matejicek, G. Mauer, A. McDonald, J. Mostaghimi, S. Sampath, G. Schiller, K. Shinoda, M.F. Smith, A. Ansar Syed, N.J. Themelis, F. Toma, J. Pablo Trelles, R. Vaßen, and P. Vuoristo, The 2016 thermal spray roadmap, *J. Therm. Spray Technol.*, 2016, **2016**(25), p 1376-1440. https://doi.org/10.1007/s11666-016-0473-x
24. O. Lanz, B. Gries, HVAF—Chance and Challenge for Users and for Powder Producers, in Thermal Spray 2019: Proceedings from the International Thermal Spray Conference, New Waves of Thermal Spray Technology for Sustainable Growth, by F. Azarmi, 26-29 May 2019 (Yokohama, Japan), (ASM International, 2019), https://doi.org/10.31399/asm.cp.itsc2019p0015.
25. R.K. Kumar, M. Kamaraj, S. Seetharamu, T. Pramod, and P. Sampathkumaran, Effect of Spray Particle Velocity on Cavitation Erosion Resistance Characteristics of HVOF and HVAF Processed 86WC-10Co4Cr Hydro Turbine Coatings, *J. Therm. Spray Technol.*, 2016, **25**(6), p 1217-1230. https://doi.org/10.1007/s11666-016-0427-3
26 K. Torkashvand, M. Gupta, S. Björklund, F. Marra, L. Baiamonte, and S. Joshi, Influence of Nozzle Configuration and Particle Size on Characteristics and Sliding Wear Behaviour of HVAF-Sprayed WC-CoCr Coatings, *Coat. Technol.*, 2021, **423**, p 127585. https://doi.org/10.1016/j.surfcoat.2021.127585
27 T.A. Owoseni, I. Ciudad de Lara, S. Mathiyalagan, S. Björklund, and S. Joshi, Microstructure and Tribological Performance of HVAF-Sprayed Ti-6Al-4V Coatings, *Coatings*, 2023, **13**(11), p 1952. https://doi.org/10.3390/coatings13111952
28. P. Khamsepour, J. Oberste-Berghaus, M. Aghasibeig, F. Ben Ettouil, A. Dolatabadi and C. Moreau, The Effect of Spraying Parameters of the Inner-Diameter High-Velocity Air-Fuel (ID-HVAF) Torch on Characteristics of Ti-6Al-4V In-Flight Particles and Coatings Formed at Short Spraying Distances, *J. Therm. Spray Technol.*, 2023, **32**, p 568-585. https://doi.org/10.1007/s11666-023-01535-z

29. L. Baiamonte, S. Björklund, A. Mulone, U. Klement, and S. Joshi, Carbide-Laden Coatings Deposited Usin#g a hand-Held High-Velocity Air-Fuel (HVAF) Spray Gun, *Coat. Technol.*, 2021, **406**, p 126725. https://doi.org/10.1016/j.surfcoat.2020.126725
30. C. Yang and I. Baker, Directional Recrystallisation Processing: A Review, *Int. Mater. Rev.*, 2021, **66**(4), p 256–286. https://doi.org/10.1080/09506608.2020.1819688
31. Z. Zhang, G. Chen, and G. Chen, The Effect of Drawing Velocity and Phase Transformation on the Structure of Directionally Annealed Iron, *Mater. Sci. Eng.*, 2006, **434**(1–2), p 58–62. https://doi.org/10.1080/09506608.2020.1819688
32. I. Baker and J. Li, Directional Annealing of Cold-Rolled Copper Single Crystals, *Acta Mater.*, 2002, **50**(4), p 805-813. https://doi.org/10.1016/S1359-6454(01)00384-6
33. A. Ganvir, A.R. Jahagirdar, A. Mulone, L. Örnfeldt, S. Björklund, U. Klement, and S. Joshi, Novel Utilization of Liquid Feedstock in High Velocity Air Fuel (HVAF) Spraying to Deposit Solid Lubricant Reinforced Wear Resistant Coatings, *J. Mater. Process. Technol.*, 2021, **295**, 117203. https://doi.org/10.1016/j.jmatprotec.2021.117203
34. G. Mauer, K.-H. Rauwald, Y.J. Sohn, and R. Vaßen, The Potential of High-Velocity Air-Fuel Spraying (HVAF) to Manufacture Bond Coats for Thermal Barrier Coating Systems, *J. Therm. Spray Technol.*, 2024, **33**(2), p 746–755. https://doi.org/10.1007/s11666-023-01659-2